A LASER-BASED 3D DATA ACQUISITION SYSTEM FOR THE ANALYSIS OF PAVEMENT DISTRESS AND ROUGHNESS

December 2004

JHR 04-300 Project 03-2

Bahram Javidi
Daesuk Kim
Sherif Kishk

This research was sponsored by the Joint Highway Research Advisory Council (JHRAC) of the University of Connecticut and the Connecticut Department of Transportation and was carried out at the Connecticut Transportation Institute of the University of Connecticut.

Technical Report Document Page

1. Report No.	2. Government Accession No.	3. Recipient's Catalog No.
JHR 04-300	N/A	N/A

4. Title and Subtitle	5. Report Date
A Laser-based 3D Data Acquisition System for the Analysis of Pavement Distress and Roughness	December 2004
	6. Performing Organization Code: N/A

7. Author(s)	8. Performing Organization Report No.
Bahram Javidi, Daesuk Kim, and Sherif Kishk	JHR 04-300

9. Performing Organization Name and Address	10. Work Unit No. (TRAIS)
University of Connecticut Connecticut Transportation Institute Storrs, CT 06269-5202	N/A
	11. Contract or Grant No.: JH 03-2

12. Sponsoring Agency Name and Address	13. Type of Report and Period Covered
Connecticut Department of Transportation 280 West Street Rocky Hill, CT 06067-0207	FINAL
	14. Sponsoring Agency Code: N/A

15. Supplementary Notes

N/A

16. Abstract

In this report we deal with the detection and classification of pavement cracks. Currently, ConnDOT is using Wisecrax® which is a commercial product supplied by Roadware. We develop a 3D laser based technique to detect the cracks in a certain pavement sector. We use phase shifting interferometer to store the 3D information of the pavement. Regular imaging systems are not able to estimate the crack depth. The proposed technique has the advantage of estimating the crack depth. The proposed laser based system can be used in conjunction with the Wisecrax® to improve its performance or as stand alone system. We used an improved multi scale wavelet algorithm to reduce the effect of the speckle noise.

17. Key Words	18. Distribution Statement
Crack Detection, Pavement Distress, Holography, Phase Shifting Interferometer	No restrictions. This document is available to the public through the National Technical Information Service Springfield, Virginia 22161

19. Security Classif. (of this report)	20. Security Classif. (of this page)	21. No. of Pages	22. Price
Unclassified	Unclassified	33	N/A

Form DOT F 1700.7 (8-72) Reproduction of completed page authorized

Acknowledgement

The authors are grateful for all the members of
the Division of Pavement Management and Data Services
of the Connecticut Department of Transportation
in Newington and Rocky Hill
for their help and support.
They are grateful and acknowledge assistance from Atef
Isaac and Sean Hong in completing this final report.

SI* (MODERN METRIC) CONVERSION FACTORS

APPROXIMATE CONVERSIONS TO SI UNITS

Symbol	When You Know	Multiply By	To Find	Symbol
		LENGTH		
in	inches	25.4	millimetres	mm
ft	feet	0.305	metres	m
yd	yards	0.914	metres	m
mi	miles	1.61	kilometres	km
		AREA		
in^2	square inches	645.2	millimetres squared	mm^2
ft^2	square feet	0.093	metres squared	m^2
yd^2	square yards	0.836	metres squared	m^2
ac	acres	0.405	hectares	ha
mi^2	square miles	2.59	kilometres squared	km^2
		VOLUME		
fl oz	fluid ounces	29.57	millilitres	mL
gal	gallons	3.785	Litres	L
ft^3	cubic feet	0.028	metres cubed	m^3
yd^3	cubic yards	0.765	metres cubed	m^3

NOTE: Volumes greater than 1000 L shall be shown in m^3

		MASS		
oz	ounces	28.35	grams	g
lb	pounds	0.454	kilograms	kg
T	short tons (2000 lb)	0.907	megagrams	Mg
		TEMPERATURE (exact)		
°F	Fahrenheit temperature	5(F-32)/9	Celcius temperature	°C

* SI is the symbol for the International System of Measurement

APPROXIMATE CONVERSIONS TO SI UNITS

Symbol	When You Know	Multiply By	To Find	Symbol
		LENGTH		
mm	millimetres	0.039	inches	in
m	metres	3.28	feet	ft
m	metres	1.09	yards	yd
km	kilometres	0.621	miles	mi
		AREA		
mm^2	millimetres squared	0.0016	square inches	in^2
m^2	metres squared	10.764	square feet	ft^2
ha	hectares	2.47	acres	ac
km^2	kilometres squared	0.386	square miles	mi^2
		VOLUME		
mL	millilitres	0.034	fluid ounces	fl oz
L	litres	0.264	gallons	gal
m^3	metres cubed	35.315	cubic feet	ft^3
m^3	metres cubed	1.308	cubic yards	yd^3
		MASS		
g	grams	0.035	ounces	oz
kg	kilograms	2.205	pounds	lb
Mg	megagrams	1.102	short tons (2000 lb)	T
		TEMPERATURE (exact)		
°C	Celcius temperature	1.8C+32	Fahrenheit temperature	°F

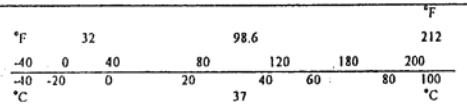

Table of Contents

List of Figures

.

List of Tables

Introduction

The researchers at the Optical/Image Processing Laboratory at the University of Connecticut (UConn), in cooperation with the Office of Research and Materials Testing and the Pavement Management Division at the Connecticut Department of Transportation (ConnDOT), have investigated image processing and recognition techniques for improving the accuracy and repeatability of the Wisecrax computer system (CCHRP Project JHR 02-11). Wisecrax automates much of the analysis of pavement distress data collected by the Automatic Road Analyzer (ARAN) vehicle. Attributes of interest include crack density, crack type (longitudinal, transverse, alligator), crack length, block cracking and crack width.

It is through this work that it has been realized that, due to the geometry of the ARAN camera set-up, the spatial resolution of the sensors are inadequate for resolving cracks at 3mm accuracy. More advanced sensors can go below this resolution. This level of accuracy is the required minimum in the American Association of State Highway & Transportation Officials' policy document Standard Practice for Quantifying Cracks in Asphalt Pavement Surface (AASHTO PP44-00). Also, the Wisecrax system itself yields a high number of false positives in identifying cracks (it identifies many cracks where there are none) and the measured widths of the cracks that it does identify correctly are unreliable and inaccurate. These problems have led ConnDOT Pavement Management to discount this width information and simply rely on crack counts and crack lengths in maintenance decisions. However, the evaluation of many pavement serviceability indices (PSI's) requires estimates of crack width to be provided. Although it is clear that the crack depth carry very valuable information regarding the pavement condition, there is no much research discussing this point. The reason behind that is that 2D intensity cameras, that are available on the markets, can not keep the depth information. Instead of estimating the crack width, we use a laser based 3D holographic imaging system to estimate the depth of the crack. The cracks depth (combined with the crack length and count) gives the information necessary to judge the pavement quality.

The main objectives of this project are the laboratory construction of a 3D laser-based range sensor and the development of algorithms for processing the data acquired from the sensor. The most common approach for acquiring such information is 3D profilometry (also known as structured light reconstruction). Here a known pattern of laser light (e.g. a grid) is projected onto the unknown surface and imaged by a Charge Coupled Device (CCD) sensor. By analyzing the deformations of this light pattern, and modeling the geometry of the projection system, 3D information can be recovered. Many other systems for 3D reconstruction that are based around similar principals such as laser-based interferometry, 3D digital holography, multiple perspective imaging, etc. Some three-dimensional image reconstruction systems are currently commercially available or can be put together using off-the-shelf products.

This project would take advantage of existing pavement distress research at UConn and collaborations with the Pavement Management Division at ConnDOT. It would complement the substantial investment by ConnDOT in Roadware technology. In addition, no changes in the current data procedures (photolog capture or WiseCrax processing) are required and no retraining of the personnel involved in these procedures is required.

1. Phase shifting holography

Digital holography [1-3] can be considered as a technique to sense and visualize 3D objects. A digital hologram contains information about different views of a 3D object so a hologram can replace a set of 2D images taken from different perspectives. In general, a digital hologram stores the complex Fresnel diffraction pattern generated by a 3D object. On-axis digital holography is easy to implement and more precise than off-axis generated digital holography. The holograms presented in this project are generated optically using phase shift interferometry [4-6] and stored in a digital computer. The 3D object reconstruction from a digital hologram is performed using digital computer by approximating the Fresnel integral digitally.

A digital hologram can be generated either using on-axis holography or off-axis holography. We use on-axis phase shifting interferometry because of its suitability for use with charged coupled device (CCD) cameras. In phase shifting digital interferometry the interference pattern between the diffraction pattern of the 3D object of interest and a reference beam is generated using CCD camera. The method relies on storing four interference patterns between the diffraction pattern of the object and the reference beam. The phase of the reference beam is different at each stored interference pattern.

To acquire the digital holograms, an optical system utilizing Mach-Zehnder interferometer is used as depicted in Fig. 1. We record the complex amplitude generated by a 3D object at a plane located at the Fresnel diffraction region.

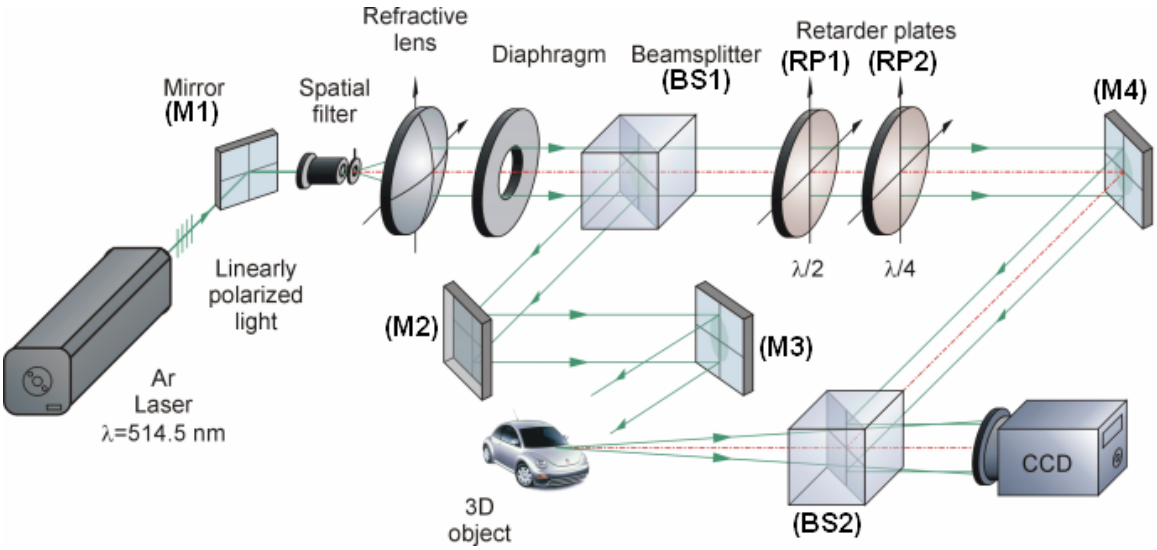

Figure 1. phase shifting interferometer

A polarized Argon laser beam of a wavelength $(\lambda = 514.5\,\text{nm})$ is divided into an object arm and a reference arm. The object beam illuminates the 3D object that diffracts light detected by a 10-bit 2048 × 2048 pixels Kodak Megaplus CCD camera, and the reference beam passes through a half-wave retardation plate RP_1 and

a quarter-wave retardation plate RP_2. The beam is polarized and can be phase modulated by rotation of the two phase retardation plates. Four phase shifts of $\alpha_n = \left\{0, \frac{\pi}{2}, \pi, \frac{3\pi}{2}\right\}$ are achieved by aligning the slow and fast axes of the two plates. Let the diffraction pattern of the 3D object, *D(x,y)*, at the CCD be given by:

$$H(x,y) = A(x,y)\exp\left(j\phi(x,y)\right) \tag{1}$$

where *A(x,y)* is the amplitude of the diffraction of the 3D object and $\phi(x,y)$ is the phase of the diffraction of a 3D object. Thus, we can record four phase-shifted interferograms given as

$$I(x,y;\alpha_n) = \left|H(x,y) + R(x,y;\alpha_n)\right|^2 \tag{2}$$

Where $H(x,y)$ is the complex amplitude distribution at the transverse coordinates (x,y) due to the object beam at the CCD plane, it is given as

$$\begin{aligned} H(x,y) &= A_H(x,y).\exp\left(i\phi_H(x,y)\right) \\ &= \frac{-i}{\lambda} \iint_{-\infty}^{\infty} U_o(x',y',z)\frac{1}{z}\exp\left(j\frac{2\pi z}{\lambda}\right).\exp\left\{\frac{j\pi}{\lambda z}\left[(x-x')^2 + (y-y')^2\right]\right\}dx'dy'dz \end{aligned} \tag{3}$$

where $U_o(x',y',z)$ is the complex amplitude distribution of the object at the coordinates (x',y',z), and z is the paraxial distance measured from the output plane.

$R(x,y;\alpha_n)$ is the complex field generated by the reference beam at the output plane, given as

$R(x,y;\alpha_n) = A_R\exp\left[i(\phi+\alpha_n)\right]$, where ϕ is the constant phase when both fast axes of the retardation plates are aligned with the direction of the polarization.

The digital hologram amplitude is calculated from the four interferometric intensity patterns as

$$A_H(x,y) = \frac{1}{4}\frac{I(x,y,0) - I(x,y,-\pi)}{\cos\left[\phi_H(x,y)\right]} \tag{4}$$

where the hologram phase $\phi_H(x,y)$ is given by

$$\phi_H(x,y) = \tan^{-1}\left[\frac{I\left(x,y,\frac{-3\pi}{2}\right) - I\left(x,y,\frac{-\pi}{2}\right)}{I(x,y,0) - I(x,y,-\pi)}\right] \tag{5}$$

The discrete complex field at any plane can be computed by numerical propagation of $H(x,y)$ using the discrete Fresnel formula

$$U(u,v)=\exp\left[-\frac{i\pi}{\lambda d}\left(\Delta x^2u^2+\Delta y^2v^2\right)\right].$$
$$\sum_{u'=0}^{N_x-1}\sum_{v'=0}^{N_y-1}H(u',v').\exp\left[-\frac{i\pi}{\lambda d}\left(\Delta x'^2u'^2+\Delta y'^2v'^2\right)\right]\exp\left[-i2\pi\left(\frac{uu'}{N_x}+\frac{vv'}{N_y}\right)\right] \quad (6)$$

where (u,v) are the reconstruction plane coordinates, (u',v') are the discrete spatial coordinates in the CCD plane, $(\Delta x',\Delta y')$ define the CCD pixel size, $(\Delta x,\Delta y)$ define the resolution of the reconstructed image, N_x and N_y are the number of columns and rows of pixels in the CCD plane.

2. Speckle noise

When using coherent light to form images, a major effect appears in the reconstructed 3D object that is called speckle noise. Due to the roughness of the surface of the object compared to the coherent light wavelength, the reconstructed 3D object will have granular appearance that looks like noise. Due to the shortage of information about the microscopic object texture, the speckle will be studied in a statistical manner. This means that even if the macroscopic details of the object are deterministic, the recorded Fresnel diffraction of the object can't be estimated precisely because of the speckle noise.

It is well known that speckle is not an additive but a multiplicative type of noise, and it occurs because of the interference patterns of randomly scattered monochromatic radiation from a surface whose roughness is of the order of the wavelength of the incident radiation. Speckle appears in images as a superimposed granular texture pattern having object-dependent properties. It significantly degrades image quality and resolution, and it becomes impossible to fully extract image details comparable in size to speckle noise. Speckle effect can be reduced by smoothing or averaging the intensity over several speckle sizes. However, if such smoothing is performed, the resolution of the image is reduced accordingly, and edge details will be wiped out. Another method for filtering out speckle noise is "Homomorphic Filtering" [7-8] which relies on performing a logarithmic transformation on the image pixels intensity values, so speckle will have an additive noise effect which can be filtered out by wiener filtering techniques.

2.1 Statistics of Speckle Noise

A granular speckle pattern—a random and chaotic signal—appears when coherent light is scattered randomly from rough surfaces. Thus, the statistics of the speckle pattern depend on the interference of the incident light and the random properties of the surfaces illuminated. It is considered as an infinite sum of independent phasors with random amplitude and phase. Fig. 2(b) clearly shows the speckle pattern in a 200×200 pixels block highlighted in Fig. 2(a). Although the block belongs to a uniform region of the car surface, speckle noise effect appears as fast spatial variation of image intensity values, causing the grainy texture shown in Fig. 2(b). Notice that speckle noise effect does not clearly appear in Fig. 2(a); this is because of the implicit

subsampling filtering performed while resizing (shrinking) this large image (2048 × 2048 pixels) to fit its allocated size in the piece of paper printed size.

As described in Appendix A, the mean and variance of the intensity value of a speckle pattern $v(x,y)$ are respectively expressed as,

$$E\{v(x,y)\} = E\{u(x,y)\}.E\{s(x,y)\} \tag{7}$$

$$\text{var}\{v(x,y)\} = \sigma_s^2.E^2\{u(x,y)\} + E\{s^2(x,y)\}\sigma_u^2 \tag{8}$$

where $v(x,y) = u(x,y).s(x,y)$, $u(x,y)$ is the original signal and $s(x,y)$ is the noise random process. E[.] stands for mean and σ^2 stands for the variance.

As can be asserted by the first term of the summation in Eq. 8, influence of speckle noise is greater in brighter regions of the image. Hence, it becomes harder to process speckle noise for our holographic images; since they are large in size (2048 × 2048 pixels), and illumination considerably varies throughout the whole image.

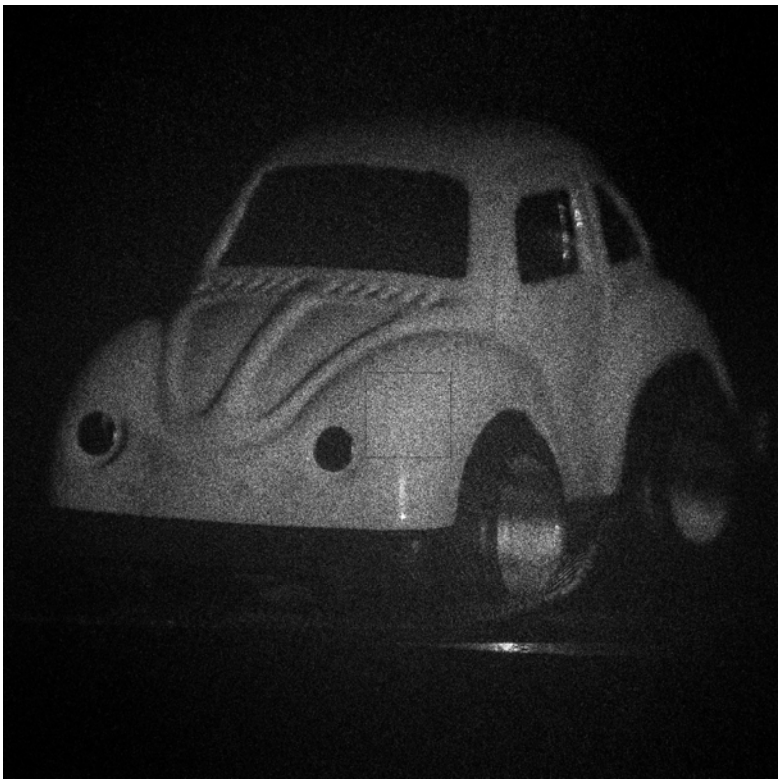

(a)

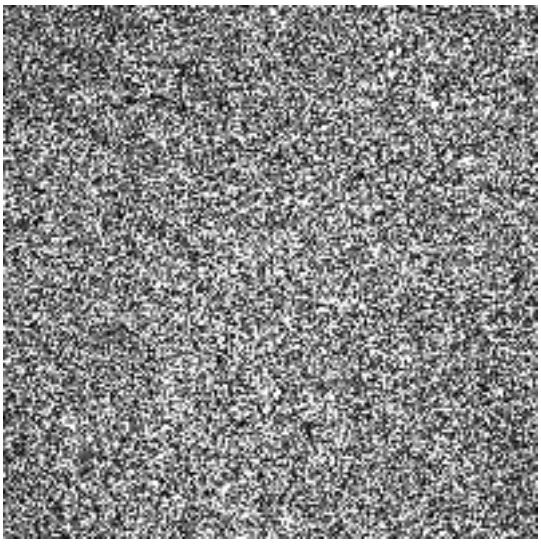

(b)

Figure 2. (a) A (2048 × 2048) pixels digital holographic image reconstructed from a digital hologram; (b) a (200 × 200) pixels block (highlighted in Fig. 2.a), showing the adverse effect of speckle noise causing the grainy texture in the image uniform regions.

3. The Wisecrax® integrated software

Wisecrax® provides a comprehensive suite of tools for the automated detection and classification of pavement distress in photolog images. These images are collected by the ARAN vehicle using two downward facing, rear-mounted cameras. To ensure that each frame records a different section of road, the frame rates of the cameras are varied dynamically based on the vehicles speed. High-powered strobe lights are used to eliminate shadows due to overhead power-lines, trees, etc. The video streams from both cameras are interleaved and recorded for offline processing. The images were interweaved during the acquire step of the processing in the office. The Wisecrax® workstation demultiplexes these two streams and combines them to provide a single continuous image of the lane. Each camera creates a 1.5 by 2 meters image, which can be combined to construct the whole image of the curb. Each continuous image can be 10 meters, 20 meters, or $1/100^{th}$ of a mile each with a width of approximately 4 meters. When detecting cracks, Wisecrax® can operate in a number of modes. The most important of these is batch mode where Wisecrax® processes a large (up to 40km) portion of road without human intervention. Human intervention is needed in the initial setting and quality control checking. The output of Wisecrax® is a crack map for each section of road and statistics summarizing the pavement condition.

The S-VHS Tape has been replaced with digital cameras to enhance the quality of the images and eliminate old VHS recorder/players equipment and associated multi connections, which reduced the image quality with each connection since the initial research was conducted.

4. Conventional Edge Detectors for Speckled Images

In this section, we will review two conventional edge detectors for speckled images, and their drawbacks will be described.

Fig. 3(b) shows the result of an attempt to detect edges of the image in Fig. 3(a) using the Canny edge detection method [9]. Speckle manifests itself as false edges picked up all over the image, especially in the brighter regions.

4.1 *CoV* Edge Detector

In the coefficient of variation *(CoV*) edge detector, the edge criterion *CoV* is defined as

$$CoV = \frac{\sigma}{\mu} \tag{9}$$

where μ, σ^2 are respectively the mean and variance of pixels intensity values over a window of a predetermined size.

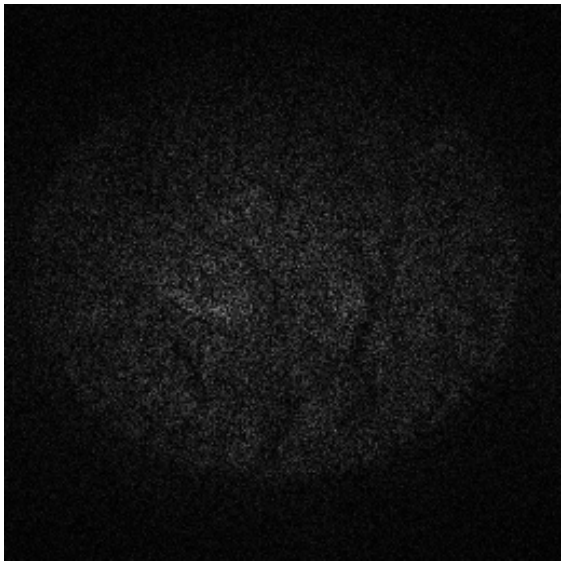

(a)

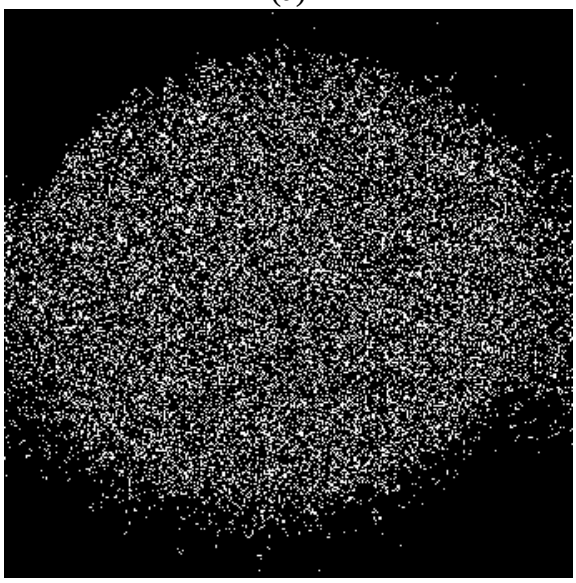

(b)

Figure 3. (a) The holographic image of a pavement. (b) Edges detected in the image shown in Fig. 3(a) using the Canny edge detection method.

The *CoV* is independent of the local average power in the homogeneous regions. From Eq. (9), the *CoV* is distributed around $\frac{1}{\sqrt{L}}$, where L is the number of looks, but the theoretical distribution of the *CoV* for a homogeneous area is not known. We can postulate that the larger the *CoV* , the stronger likelihood that the neighborhood belongs to an edge. However, a fixed threshold for optimum edge detection can not be determined theoretically. For our holographic single-look images, the center pixel of a local window is determined to belong to the homogeneous area if the *CoV* is less than a threshold value; otherwise, to the edge region. Although this method does not depend on the average intensity of the noisy image, our experiments have shown that it misses many significant edges in coherent holographic images. Figures 4.a, 4.b, and 4.c show the edges detected using *CoV* threshold values of 1.0, 1.05, and 1.1, respectively. It is evident that most of the detected edges are due to the inherent presence of speckle noise, and most of the significant true edges are left undetected.

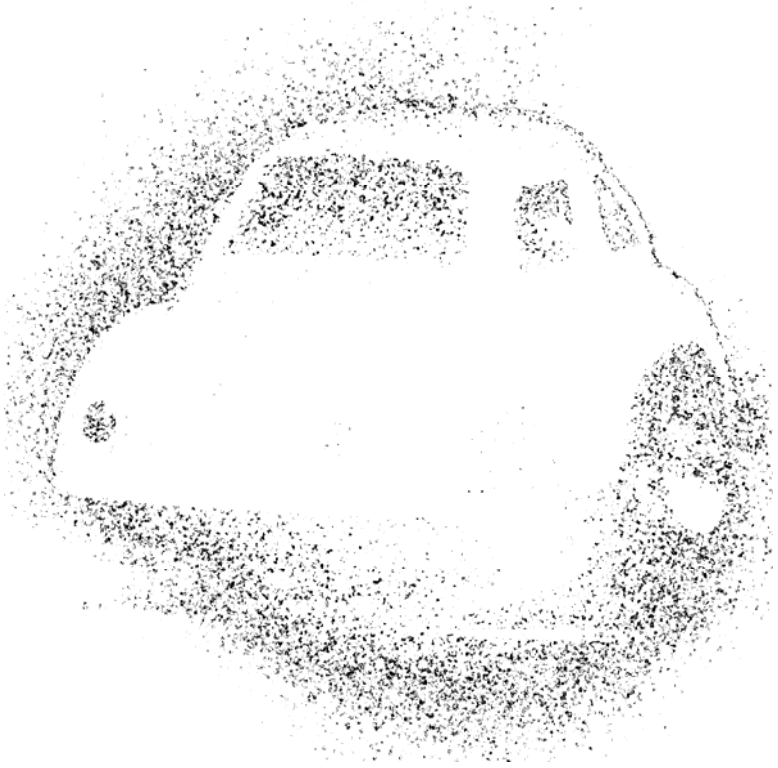

(a)

(b)

(c)

Figure 4(a)-(c) Edges detected in the image shown in Fig. 2(a) using the *CoV* method with thresholds of 1.00, 1.05, 1.10, respectively.

4.2 LoG-RoA Edge Detector

In the "Laplacian of Gaussian – Ratio of Averages" *(LoG-RoA)* edge detector, zero crossing (ZC) points are detected first by applying the *LoG* operator to the holographic image. Responding to multiplicative noise, the *LoG* operator detects many unnecessary ZC points in the homogeneous regions; so it can not be used independently as an edge detector for speckled holographic images. Therefore, in the *LoG-RoA* edge detector the operator based on the *RoA* is also used. That is, the edge magnitude RoA(i, j) at (i, j) is given by the root mean square of the horizontal edge component H(i, j) , and the vertical edge component V(i, j) , i.e.,

$$RoA(i,j) = \left[H^2(i,j) + V^2(i,j)\right]^{\frac{1}{2}} \tag{10}$$

where $H(i,j)$ is defined as $\max\left[\frac{R(i,j)}{L(i,j)}, \frac{L(i,j)}{R(i,j)}\right]$, $R(i,j)$ and $L(i,j)$ are average values over neighborhoods on the right and left through the center of a window, respectively. The vertical edge component $V(i,j)$ is defined similarly for the neighborhoods above and below the center of a window.

To obtain the final edge map, the ZC points obtained by the *LoG* operator are compared with the selected edge candidates obtained by the *RoA* operator. Generally, ZC contours show many false edges in the homogeneous region, but they entail a dead zone near real edges where no ZC points are detected. On the other hand, the *RoA* operator eliminates many false edges in the homogeneous region, but the detected edges are usually more than one pixel wide. Thus, with the logical AND operation on the candidate points detected by the *LoG* and *RoA* operators, the final one-pixel wide edge map is obtained. As experimental results show in Fig. 5, this procedure performs poorly when applied to coherent holographic images.

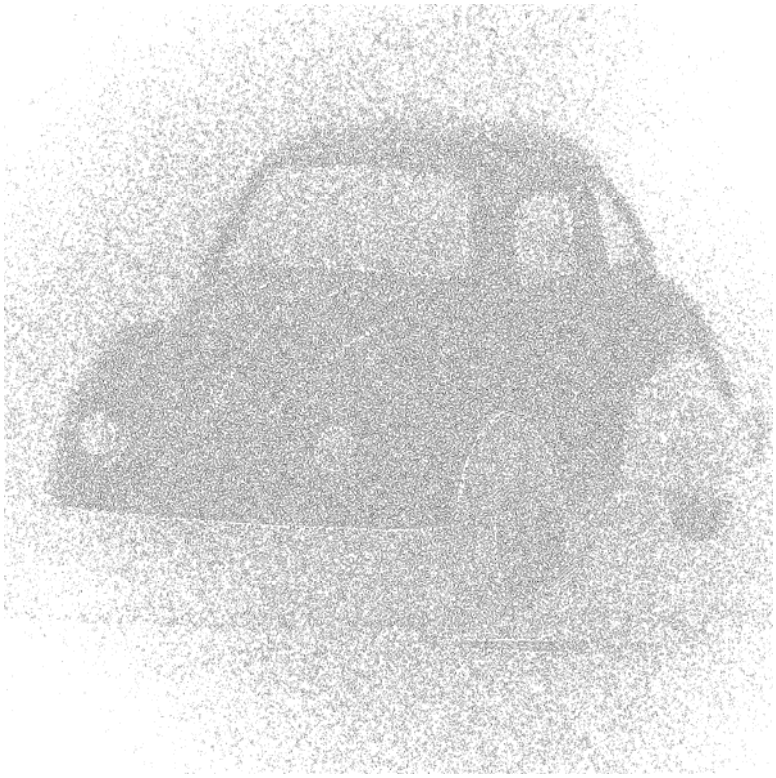

Figure 5. Edges detected in the image shown in Fig. 2(a) using the Laplacian of Gaussian – Ratio of Averages method.

5. The dyadic wavelet transform

Mallat [10] proved that the modulus of the local maxima of the wavelet transform of a signal correspond to the signal's sharp variations at the same locations. He provided numerical procedures to characterize those sharp variations based on the evolution across the scales of the wavelet transform at these modulus maxima locations. Thus speckle noise can be discriminated from important true edges through an analysis of the wavelet transform modulus maxima behavior along different scales.

5.1 The wavelet transform modulus maxima

As a multiscale version of the Canny edge detector, two mother wavelet functions are defined as

$$\psi^1(x,y) = -\frac{\partial\theta(x,y)}{\partial x} \quad \text{and} \quad \psi^2(x,y) = -\frac{\partial\theta(x,y)}{\partial y} \tag{11}$$

which are the partial derivatives of a two-dimensional smoothing function $\theta(x,y)$ along x and y, respectively.

The dilation by a scaling factor s of the above wavelets is given by:

$$\psi_S{}^1(x,y) = \left(\frac{1}{s}\right)^2 \psi^1\left(\frac{x}{s},\frac{y}{s}\right) \quad \text{and} \quad \psi_S{}^2(x,y) = \left(\frac{1}{s}\right)^2 \psi^2\left(\frac{x}{s},\frac{y}{s}\right)$$

For any 2-D square-integrable function $f(x,y) \in L^2(R^2)$, where R is the set of all real numbers, the wavelet transform at scale s has two components defined as:

$$\begin{pmatrix} W^1 f(s,x,y) \\ W^2 f(s,x,y) \end{pmatrix} = s \begin{pmatrix} \frac{\partial}{\partial x}(f * \theta_s)(x,y) \\ \frac{\partial}{\partial y}(f * \theta_s)(x,y) \end{pmatrix} = s\vec{\nabla}(f * \theta_s)(x,y) \qquad (12)$$

where "$*$" denotes convolution, and $\vec{\nabla}$ is the gradient operator.
For less computational time, the dilation parameter s is allowed to change only along the dyadic sequence $(2^j)_{j \in z}$, where z is the set of all integer numbers. Digital images are sampled at a finite resolution, below which we can not compute the wavelet transform. Therefore, the finest scale is normalized to 1, and a scaling function $\phi(x,y)$ is introduced whose Fourier transform is an aggregation of the wavelet components dilated by scales 2^j larger than 1:

$$\left|\hat{\phi}(\omega_x,\omega_y)\right|^2 = \sum_{j=1}^{\infty} \hat{\psi}^1(2^j\omega_x, 2^j\omega_y)\hat{\chi}^1(2^j\omega_x, 2^j\omega_y) + \hat{\psi}^2(2^j\omega_x, 2^j\omega_y)\hat{\chi}^2(2^j\omega_x, 2^j\omega_y) \qquad (13)$$

where $\chi^1(x,y), \chi^2(x,y)$ are the reconstructing wavelets satisfying

$$f(x,y) = \sum_{j=-\infty}^{\infty} \left(W^1 f(2^j,x,y) * \chi^1(2^j,x,y) + W^2 f(2^j,x,y) * \chi^2(2^j,x,y)\right) \qquad (14)$$

By defining the modulus of the gradient vector at scale 2^j as $Mf(2^j,x,y) = \sqrt{\left|W^1 f(2^j,x,y)\right|^2 + \left|W^2 f(2^j,x,y)\right|^2}$, and the direction of the gradient vector, which is also the angle of the gradient vector $\vec{\nabla}(f * \theta_s)(x,y)$, as $Af(2^j,x,y) = \tan^{-1}\left(\frac{W^2 f(2^j,x,y)}{W^1 f(2^j,x,y)}\right)$, we can extend the Canny edge detector algorithm to a multiscale implementation. The sharp variation points of $f * \theta_{2^j}(x,y)$ are the points (x_o, y_o) where the modulus of the gradient vector $(Mf(2^j,x,y))$ is maximum in the direction of the gradient vector $(Af(2^j,x,y))$, which indicates where the image has the sharpest variation.

5.2. Lipschitz exponents and irregularities discrimination

Each irregular pixel, a discontinuity in the image pixels intensity, produces modulus maxima values at different scales (2^j). Those values can be used to estimate the local regularity at that pixel. In mathematics, Lipschitz exponents are used to measure the local regularity of functions, and it can be measured from the evolution across scales of the absolute value of the wavelet transform. Speckle noise and important edges, though both are considered to be irregularities in the image intensity, but they have different evolution behaviors across the scales of the wavelet

transform local maxima, and thus they will have different Lipschitz exponents. So, if we can measure the Lipschitz exponents at the wavelet transform local maxima locations, we will be able to distinguish important edges from speckle noise.

5.3 Characterization of local regularity (Lipschitz exponents determination)

Meyer [11] had proven that a two dimensional function $f(x,y) \in L^2(R^2)$ is Lipschitz α, $0 < \alpha < 1$ over $]a+\varepsilon, b-\varepsilon[\times]c+\varepsilon, d-\varepsilon[$, if and only if for any $\varepsilon > 0$ there exists a constant A_ε such that for $(x,y) \in]a+\varepsilon, b-\varepsilon[\times]c+\varepsilon, d-\varepsilon[$, and at any scale 2^j, the following condition holds

$$Mf(2^j, x, y) \le A_\varepsilon (2^j)^\alpha \qquad (15)$$

where $Mf(2^j, x, y)$ is the modulus of the wavelet transform at scale 2^j at location (x, y).

Taking the log of (15), we have

$$\log_2(Mf(2^j, x, y)) \le \alpha j + \log_2(A_\varepsilon) \qquad (16)$$

So, the Lipschitz exponents can be estimated by measuring the decay slope of $\log_2(Mf(2^j, x, y))$ as a function of j. In the homogeneous regions which contain speckle noise, the modulus local maxima decay abruptly with increasing the scale, they are characterized by negative Lipschitz exponents, which means that they are more likely to be singularities, not discontinuities in the image intensity. On the contrary, those modulus local maxima which represent important edges, persist across the scales of the wavelet transform, implying positive Lipschitz exponents, and that they represent true edges.

6. Cracks depth estimations

One important parameter in characterizing the crack severity is the crack depth. Regular imaging systems are not able to detect the crack depth. Using 3D digital holography imaging we make an estimate of the crack depth. In digital holography, the areas reconstructed at their actual distance from the CCD will be focused and other areas will be out of focus. Figure 7 shows a pavement images reconstructed at different distances using inverse Fresnel diffraction. Even thought the difference is not very obvious, visually, in figure 6, the edge detection algorithm we use extracted the changes in the focused areas between the different reconstruction distances. Using this technique, we can make a rough estimate for the crack depth that can be used to judge the severity of the crack.

To find the depth of the crack we reconstruct the three dimensional pavement using the stored hologram, then we find the reconstruction distanced that gives the best focus at the cracks areas. We use texture detection techniques to find the texture strength and use this to measure how the area is focused [12]. Figure 7 shows a block diagram for the proposed crack depth estimation algorithm. As shown in figure 7 we can use either the output of the Wisecrax system or use this system as a stand-alone system. We apply the texture detection technique to the areas identified by the Wisecrax system to find the distance of the crack from the recording camera, and use this to estimate the crack depth.

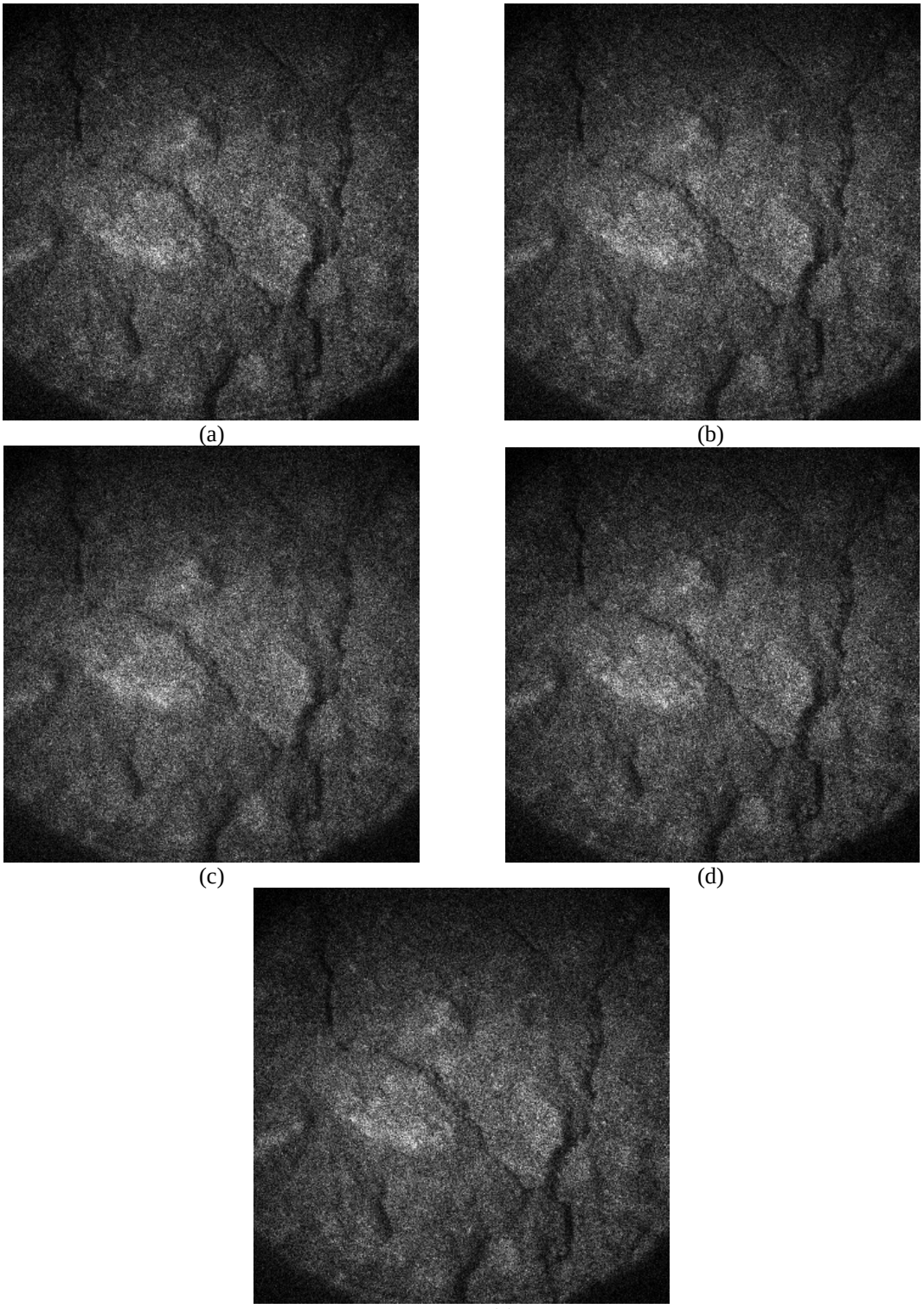

(a) (b) (c) (d) (e)

Figure 6. The holographic image of a pavement reconstructed at a distance of (a) 830 mm (b) 832.5mm (c) 835 mm (d) 837.5 mm (e) 840 mm

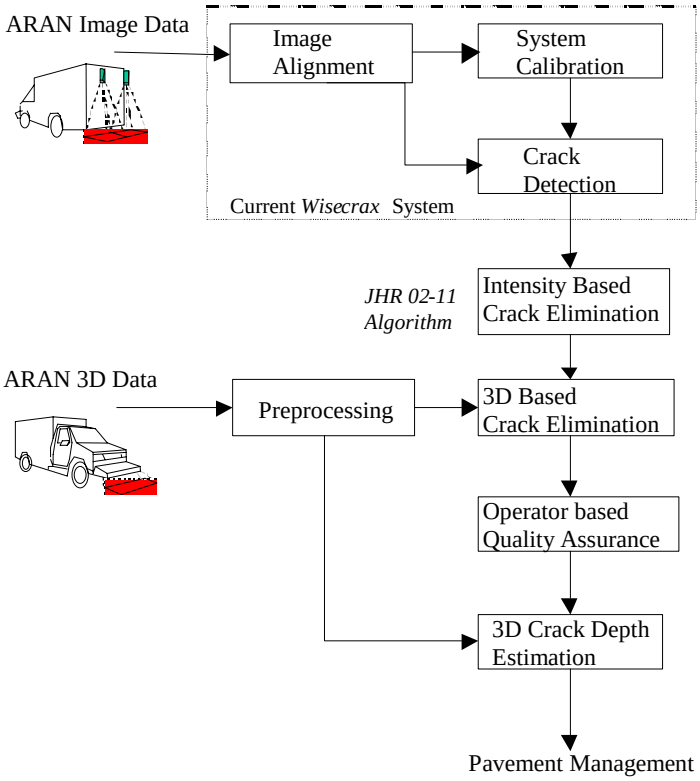

Figure 7. Block diagram for the proposed system

We use the multi-scale edge detection technique and apply it to the identified cracked areas. We use a moving averaging kernel to reduce the effect of noise. An image pixel reconstructed at a certain distance that gives the highest output will be considered at the corresponding distance. This will be applied to each pixel in the cracked areas.

7. Implementation and Results

Two-dimensional quadratic spline wavelets, which are the first derivative of the cubic spline, were used to implement the fast discrete wavelet transform. The quadratic spline wavelet is anti-symmetric, regular and of compact support. Discrete FIR filter banks are implemented for each of the two dimensions, as will be shown, to calculate the fast dyadic wavelet transform. Interested readers should refer to Appendix B for a derivation of the filters' design procedure for constructing the scaling and wavelet functions.

For discrete implementation, at any scale 2^j, each pixel $s_j[m,n]$ of the approximation image $S_{2^j} f(x,y)$ is an averaging of $f(x,y)$ with the scaling function $\phi_{2^j}(x)\phi_{2^j}(y)$ translated at $[m,n]$, i.e.

$$s_j[m,n] = \left\langle f(x,y), \phi_{2^j}(x-m)\phi_{2^j}(y-n) \right\rangle \qquad (17)$$

For simplicity, this can be expressed for one dimension in the convolution form as

$$s_{j+1}[n] = f * \bar{\phi}_{2^{j+1}}(n) \qquad (18)$$

where $\bar{\phi}_{2^j}(n) = \phi_{2^j}(-n)$

The $w_{j+1}[n]$ pixel of the details image at scale 2^{j+1}, in either the horizontal or vertical direction is computed with a similar convolution as

$$w_{j+1}[n] = f * \bar{\psi}_{2^{j+1}}(n) \tag{19}$$

where $\bar{\psi}_{2^j}(n) = \psi_{2^j}(-n)$

The Fourier transforms of the sampled signals $s_{j+1}[n], w_{j+1}[n]$ are

$$\hat{s}_{j+1}(\omega) = \sum_{k=-\infty}^{\infty} \hat{f}(\omega + 2k\pi)\hat{\phi}^*_{2^{j+1}}(\omega + 2k\pi) \tag{20}$$

$$\hat{w}_{j+1}(\omega) = \sum_{k=-\infty}^{\infty} \hat{f}(\omega + 2k\pi)\hat{\psi}^*_{2^{j+1}}(\omega + 2k\pi) \tag{21}$$

Substituting in (20) and (21) from (b-4) and (b-6) we get

$$\hat{s}_{j+1}(\omega) = H(2^j\omega)\hat{s}_j(\omega) \tag{22}$$

$$\hat{w}_{j+1}(\omega) = G(2^j\omega)\hat{s}_j(\omega) \tag{23}$$

Taking the inverse Fourier transform of (22), (23)

$$s_{j+1}[n] = h_j * s_j[n] \tag{24}$$

$$w_{j+1}[n] = g_j * s_j[n] \tag{25}$$

where $h_j[n]$ and $g_j[n]$, the inverse Fourier transforms of $\hat{H}(2^j\omega)$ and $\hat{G}(2^j\omega)$, are the discrete filters obtained by expansion of the impulse responses of $h[n]$ and $g[n]$ by a factor of 2^j. Two dimensional filtering is obtained by convolving the rows and columns of the image $f(x,y)$ with the one dimensional filters $h_j[n]$, $g_j[n]$ derived in Appendix B.

The discrete wavelet decomposition of the image approximation at scale 2^j, $S_{2^j} f(x,y)$, is decomposed to the approximation image at the coarser scale $S_{2^{j+1}} f(x,y) = S_{2^j} f(x,y) * h_j(x) * h_j(y)$, and the two image details $W^1_{2^{j+1}} f(x,y) = S_{2^j} f(x,y) * g_j(x)$ and $W^2_{2^{j+1}} f(x,y) = S_{2^j} f(x,y) * g_j(y)$.

Starting with the original image, the procedure is repeated recursively to get all the approximation images $S_{2^j} f(x,y)$ up to the coarsest scale 2^J. The details images $W^1_{2^{j+1}} f(x,y)$, and $W^2_{2^{j+1}} f(x,y)$ are obtained by convolving the approximation images $S_{2^j} f(x,y)$ with the respective high pass filters $g_j(x)$ and $g_j(y)$. Fig. 8 shows a block diagram of the filter banks realization involved in computing the approximations and details images.

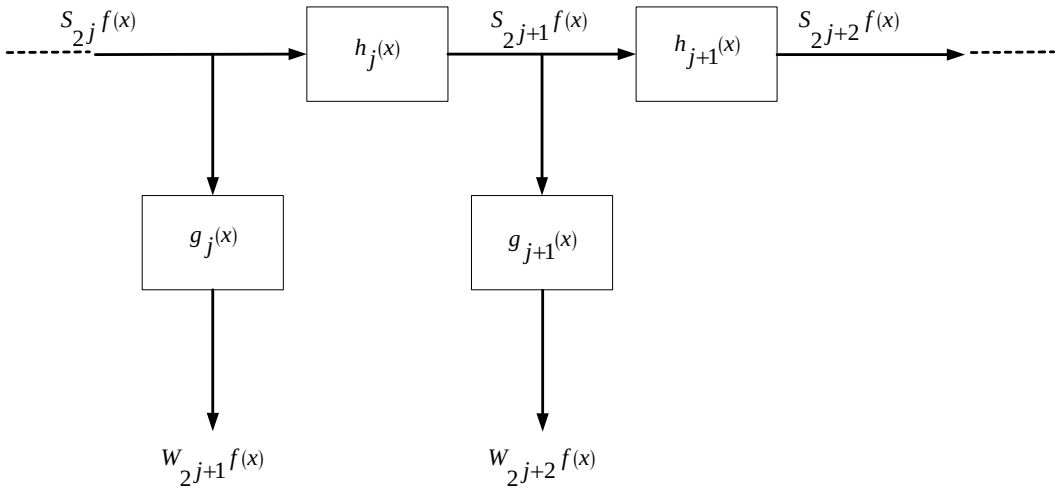

Figure 8. 1-D discrete filter banks realization for computing the fast dyadic wavelet transform.

Like in the canny edge detector, for each scale 2^j, we compute $Mf\left(2^j, x, y\right)$, and $Af\left(2^j, x, y\right)$, the local maxima of the wavelet transform are the points (x, y) where the modulus image $Mf\left(2^j, x, y\right)$ is locally maximum along the gradient direction given by $Af\left(2^j, x, y\right)$. We record the position of each of those local maxima.

Most of the important edges of the original image have positive Lipschitz exponents, which means that we can separate speckle noise from the important edges by measuring the evolution across scales of the wavelet transform maxima, i.e. the Lipschitz exponents. Also, knowledge of the geometrical properties of the important edges can also be used to connect modulus maxima points which belong to smooth maxima edge curves, i.e. two adjacent local maxima points are connected together if their respective position is perpendicular to the direction indicated by $Af\left(2^j, x, y\right)$, and the modulus $Mf\left(2^j, x, y\right)$ of the two maxima have close values. On the contrary, the sharp variation points of speckle noise have negative Lipschitz exponents, and the modulus maxima values $Mf\left(2^j, x, y\right)$ of two adjacent local maxima points do not have close values, hence they do not create such smooth curves of $Mf\left(2^j, x, y\right)$, and they can be easily discriminated.
Figure 9(b) to 9(e) shows the edge detected at different scales for the holographic image shown in figure 9(a). The amplitude of the maxima are severely affected by speckle noise at the finer scales, but when looking at coarser scales, the effect of important edges more clearly appears.

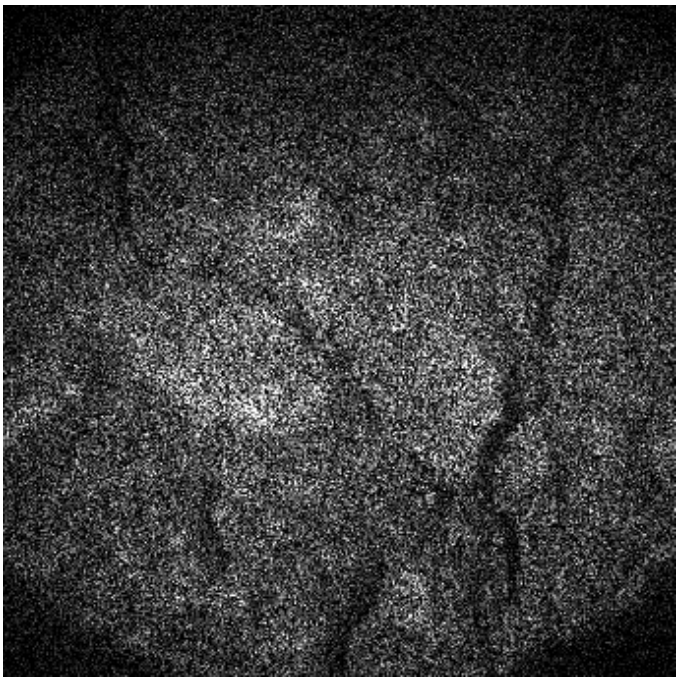

(a)

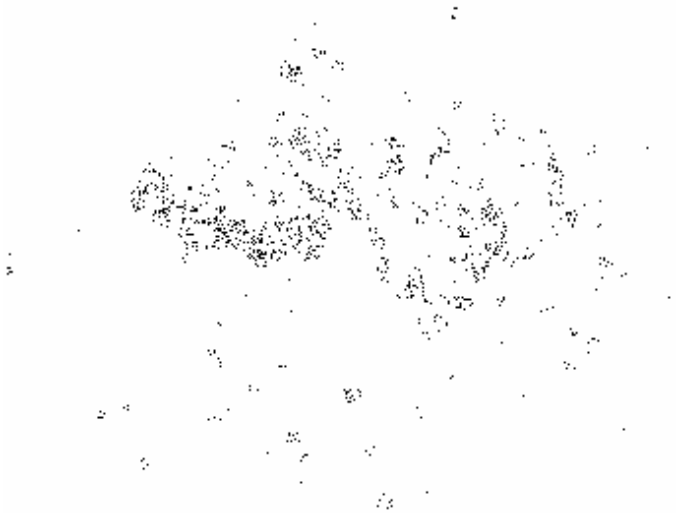

(b)

(c)

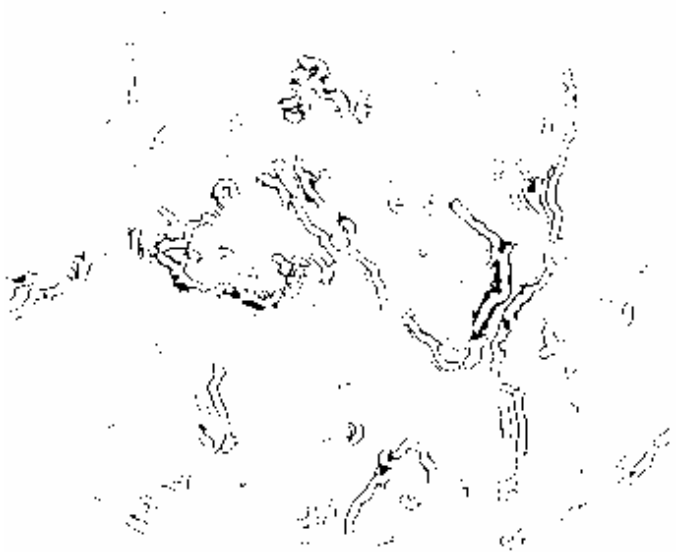

(d)

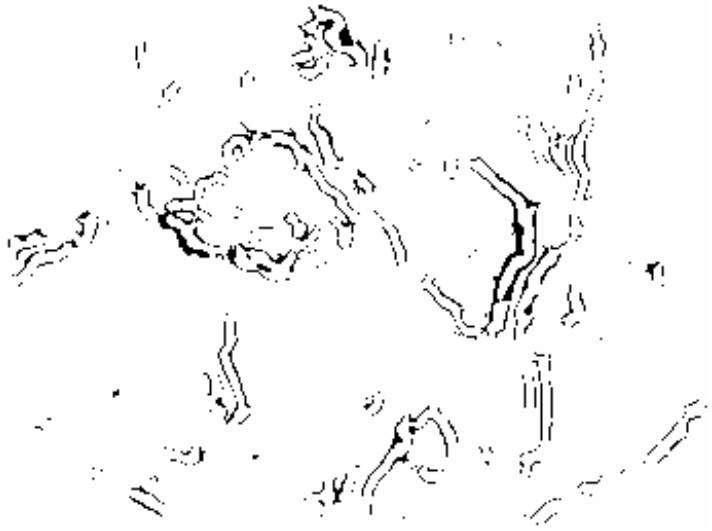

(e)

Figure 9. (a) Three dimensional holographic image for a pavement sector. (b-e) The detect cracks using different scales using a relatively low threshold.

To remove speckle noise components, we suppress all the maxima points which propagate with a Lipschitz exponent less than –a certain threshold; since they imply that their amplitude increases when the scale decreases, which is a characteristic of speckle noise. The Lipschitz exponents are computed from the evolution of the wavelet transform local maxima across the scales $2^1, 2^2, 2^3$ as was mathematically described in Eq. (16). At the coarsest scale, we suppress modulus maxima which are less in value than a certain threshold, and all modulus maxima in the finer scales which propagate to them.

We use the either the previous crack locations estimations or the Wisecrax results and estimate the depth of the cracked areas. We use a pavement that stored using holographic imaging at a distance of 830mm from the CCD. We reconstruct the 3D image at distances of 830, 832.5, 835, 837.5, and 840 mm. We relate each pixel to the level that provides the best focusing. In reality a crack doesn't have a fixed depth but a fluctuating depth and width. So, to evaluate the severity of the crack we use the mean depth, the maximum depth, and the standard deviation of the calculated depth. Figure 10 shows the calculated cracks for the pavement shown in Figure 9 (a), notice that we use a clustering technique that connects the point that may be related to the same crack.

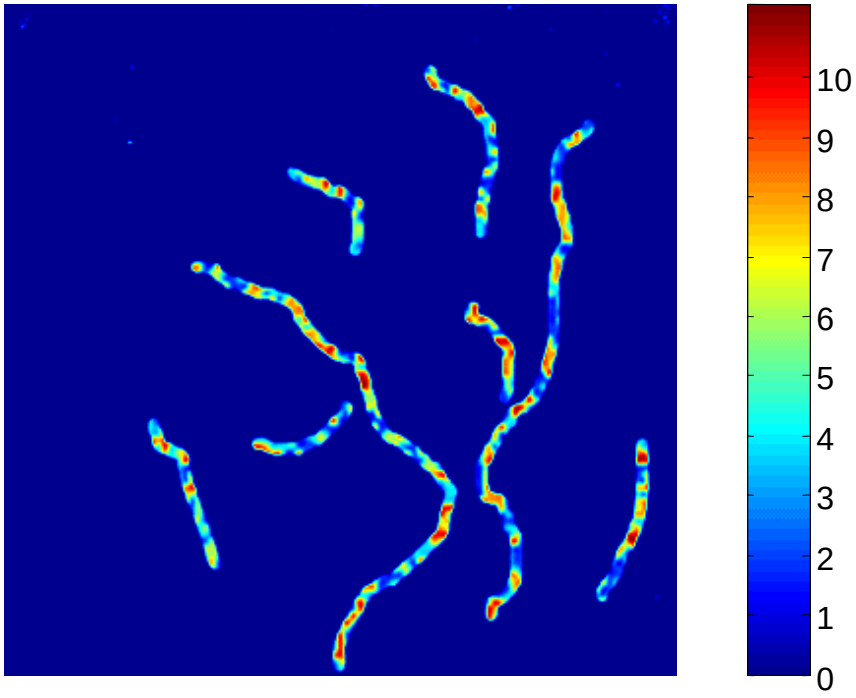

Figure 10. Color mapping for the depth of the cracks for the pavements shown on Figure 9(a)

We use a *k* mean clustering algorithm to separate each crack then measure its parameters which include maximum depth, average depth and the mean depth and use this information in combination with the results of the Wisecrax system to judge the quality of the pavement. Table 1 shows the computed mean crack depth, standard deviation and maximum crack depth for the cracks on figure 10.

Table 1. Details for the cracks in figure 10

Crack location(x,y)	789.5229 865.180	416.9393 455.6941	694.1301 341.5548	787.4711 610.9246	544.4982 763.8613	295.5051 800.5007	158.7225 691.7868
Mean depth (mm)	3.2964	4.7967	4.4524	5.7523	5.3498	4.1341	4.5478
Standard deviation-mm	2.5004	2.3945	2.2519	2.4725	2.6398	2.3528	2.4987
Maximum depth-mm	11.0717	11.2479	11.2479	10.1325	10.9318	8.3524	9.8262

Conclusion

In this project we proposed a 3D laser based imaging system that can be used for pavement distress. The proposed system can be used in conjunction with the Wiscrax system. A multi-scale wavelet technique is used to estimate the depth of the crack from the stored holographic images. The fusion between the holographic image and the Wisecrax image gives more accurate information about the crack and helps to evaluate the pavement condition. The present system is too large and sensitive to be installed on a moving van because of the high power laser source and the interferometer. We need to find more robust 3D imaging systems to be able to place them on a moving platform

References

1- H. J. Caulfield, *Handbook of Optical Holography*, Academic, London, 1979.
2- J. W. Goodman, *Introduction to Fourier Optics*, McGraw-Hill, New York, NY, 1996.
3- U. Schnars, and W. P. O. Jüptner, ”Direct recording of holograms by a CCD target and numerical reconstruction” Appl. Opt. Vol. **33**, 179-181 (1994).
4- I Yamaguchi, and T Zhang, ”Phase-Shifting Digital Holography” Opt. Lett. Vol. **22**, 1268-1270 (1997)
5- J. H. Bruninig, D. R. Herriott, J. E. Gallagher, D. P. Rosenfeld, A. D. White, and D. J. Brangaccio, “Digital Wavefront measuring interferometer for Testing Optical Surfaces and Lenses,” Appl. Opt. **13**, 2693 (1974).
6- J. Schwider, “Advanced Evaluation Techniques in Interferometry,” in *Progress in Optics*, E. Wolf, ed (North Holland, Amesterdam) Vol. **XXVIII**, 271-359 (1990).
7- Anil Jain, *Fundamentals of Digital Image Processing*, Englewood Cliffs, NJ: Prentice Hall Press, (1989).
8- Anil Jain and Charles Christensen, "Digital processing of images in speckle noise," *Proc. SPIE, Applications of Speckle Phenomena* 243, 46-50 (July 1980).
9- J. Canny, "A computational approach to edge detection,” IEEE Trans. on Pattern Analysis and Machine Intelligence, vol. 8, pp. 679-698 (1986).
10- Stephan Mallat, *A Wavelet Tour of Signal Processing*, Academic Press, (1999).
11- Y. Meyer, *Wavelets and Operators*, Cambridge University Press, (1992).
12- B. Javidi, *Image Recognition and Classification: Algorithms, Systems, and Applications*, Marcel Dekker, New York (2002)

Appendix A

Speckle noise statistics

Speckle noise is considered as an infinite sum of independent phasors with random amplitude and phase. This yields a representation of its complex amplitude as:

$$a(x,y) = a_R(x,y) + j a_I(x,y) \qquad \text{(A-1)}$$

where a_R, a_I are zero mean, independent Gaussian random variables with variance $\sigma_a{}^2$

The intensity is:

$$s(x,y) = |a(x,y)|^2 = a_R^2 + a_I^2 \qquad \text{(A-2)}$$

and it has an exponential probability density function,

$$f(s) = \frac{1}{2\sigma_a^2} \exp\left(\frac{-s}{2\sigma_a^2}\right), \qquad \text{(A-3)}$$

With mean and variance given by:

$$\mathrm{E}\{s\} = 2\sigma_a^2 \qquad \text{(A-4)}$$

$$\sigma_s^2 = 2\sigma_a^2 \qquad \text{(A-5)}$$

Even though a speckle pattern has no detailed information about the structure of the surface of an illuminated object, it is well described by its *pdf*. In general, a speckle pattern $v(x,y)$ is modeled by the multiplication of an original signal $u(x,y)$ and a noise random process $s(x,y)$

$$v(x,y) = u(x,y).s(x,y) \qquad \text{(A-6)}$$

Generally, at a certain pixel (x,y), the original image and speckle noise intensity values are independent of each other, the mean and variance of the intensity value at (x,y) are respectively expressed as,

$$E\{v(x,y)\} = E\{u(x,y)\}.E\{s(x,y)\}$$

$$\mathrm{var}\{v(x,y)\} = E\left\{\left(v(x,y) - E\{v(x,y)\}\right)^2\right\} = \sigma_s^2.E^2\{u(x,y)\} + E\{s^2(x,y)\}\sigma_u^2$$

where $E\{\cdot\}$ is the expectation, and σ_u^2, σ_s^2 are the variances of $u(x,y)$, $s(x,y)$, respectively.

The term $\sigma_s^2.E^2\{u(x,y)\}$ clarifies the fact that the influence of speckle noise is greater in the brighter regions.

Appendix B

Spline wavelets filters design

The continuous cubic spline is the convolution of four box functions, it has two continuous derivatives, abrupt jumps in the third derivative, and a sequence of delta functions in the fourth derivative.
The box function has a Fourier transform which is a sinc function, thus

$$\hat{B}(\omega)=\left(\frac{\sin\left(\frac{\omega}{2}\right)}{\frac{\omega}{2}}\right) \tag{b-1}$$

We take the scaling function $\phi(x)$ as a box spline of degree 2. The Fourier transform of $\phi(x)$ is the multiplication of three sinc functions given as:

$$\hat{\phi}(\omega)=e^{\frac{-i\omega}{2}}\left(\frac{\sin\left(\frac{\omega}{2}\right)}{\frac{\omega}{2}}\right)^3 \tag{b-2}$$

The phase shift $e^{-\frac{i\omega}{2}}$ is a consequence of $\phi(x)$ being centered at $x=\frac{1}{2}$.
From the multi-resolution causality property [10], the dilation by a factor of 2 of the scaling function, $\phi\left(\frac{x}{2}\right)$, must be a combination of the basis functions $\phi(x-n)$.
Hence, a discrete filter $h[n]$ that relates both is given as:

$$h[n]=\left\langle\frac{1}{\sqrt{2}}\phi\left(\frac{x}{2}\right),\phi(x-n)\right\rangle \tag{b-3}$$

which can be expressed in the frequency domain as:

$$\hat{\phi}(2\omega)=\frac{1}{\sqrt{2}}\hat{H}(\omega)\hat{\phi}(\omega) \tag{b-4}$$

substituting (32) into (34), we get

$$\hat{H}(\omega)=\sqrt{2}e^{-i\frac{\omega}{2}}\left(\cos\left(\frac{\omega}{2}\right)\right)^3 \tag{b-5}$$

From Eq. (35), We can get $h(n)$, the impulse response of the filter $\hat{H}(\omega)$ as the coefficients of

$$\hat{H}(\omega)=\sqrt{2}e^{-i\frac{\omega}{2}}\left(\frac{e^{i\frac{\omega}{2}}+e^{-i\frac{\omega}{2}}}{2}\right)^3=\frac{\sqrt{2}}{8}z^{-2}\left(z^3+3z^2+3z^1+1\right), \text{ where } z=e^{i\omega}$$

Thus $h[n] = \sqrt{2}\left[\frac{1}{8}, \underline{\frac{3}{8}}, \frac{3}{8}, \frac{1}{8}\right]$

So, $h[n]$ can be implemented as a low-pass FIR filter.

Imposing that the corresponding wavelet $\psi(x)$ has a Fourier transform that can be obtained as

$$\hat{\psi}(2\omega) = \frac{1}{\sqrt{2}} G(\omega)\hat{\phi}(\omega) \tag{b-6}$$

Since $\psi(x)$ is the first order derivative of a smoothing function $\theta(x)$, so it should have one zero at $\omega = 0$. Choosing $\theta(x)$ as a cubic spline smoothing function, so its Fourier transform is

$$\hat{\theta}(\omega) = \frac{-1}{4} e^{\frac{-i\omega}{2}} \left(\frac{\sin\left(\frac{\omega}{4}\right)}{\left(\frac{\omega}{4}\right)} \right)^4 \tag{b-7}$$

Consequently, the Fourier transform of $\psi(x)$ is

$$\hat{\psi}(\omega) = \frac{-1}{4} i\omega\, e^{\frac{-i\omega}{2}} \left(\frac{\sin\left(\frac{\omega}{4}\right)}{\left(\frac{\omega}{4}\right)} \right)^4 \tag{b-8}$$

Substituting (32), (38) into (36), we get

$$\hat{G}(\omega) = -i\sqrt{2} e^{\frac{-i\omega}{2}} \sin\left(\frac{\omega}{2}\right) \tag{b-9}$$

Which is a high pass filter that has one zero at $\omega = 0$

From (39), We can get $g(n)$, the impulse response of the filter $\hat{G}(\omega)$ as the coefficients of $\hat{G}(\omega) = -\sqrt{2} i e^{\frac{-i\omega}{2}} \left(\frac{e^{\frac{i\omega}{2}} - e^{\frac{-i\omega}{2}}}{2i} \right) = \frac{-1}{\sqrt{2}} \left(1 - z^{-1}\right)$

So, $g[n] = \left[-\frac{1}{\sqrt{2}}, \underline{\frac{1}{\sqrt{2}}} \right]$ (b-10)

Which is a finite difference filter approximating a derivative.